OPEN ACCESS
JOURNAL OF ADVANCED DIELECTRICS
2550040 (13 pages)

DOI: 10.1142/S2010135X25500407

Early diagnosis of breast cancer with a highly accurate dual-band graphene-based refractive index sensor

Seyed Amin Khatami, Pejman Rezaei* and Mohammad Danaie
Electrical and Computer Engineering Faculty
Semnan University, Semnan, Iran
*prezaei@semnan.ac.ir

Received 21 July 2025; Revised 2 December 2025; Accepted 29 December 2025; Published 31 January 2026

This study presents a precise refractive index (RI) sensor based on a dual-band graphene-based absorber for the early diagnosis of breast cancer. The sensor exhibits two strong absorption peaks at 4.58 THz and 6.25 THz, with efficiencies of 99.99% and 90%, respectively. Full-wave simulations and a transmission line model were used to assess the sensor's performance, showing strong consistency. The sensor detects variations in the analyte's RI, achieving a sensitivity of up to 2.22 THz/RIU and a Figure of Merit (FoM) of 7.7 RIU^{1}. The use of a top-gate structure allows dynamic tuning of graphene's chemical potential, enhancing adaptability. While the study is simulation-based and lacks experimental validation, it demonstrates the potential of this sensor for detecting biological changes, including those associated with breast cancer cells (RI range of 1.3 to 1.4). The simulation was performed using CST software with the FDTD solver. Future experimental validation will be necessary to confirm the device's real-world applicability.

Keywords: Dual-band absorber; refractive index sensor; terahertz frequency; graphene; breast cancer; metamaterials.

1. Introduction

The THz band, encompassing the range of frequencies from 0.1 to 10 THz, has attracted significant attention from many researchers in recent years. Consequently, numerous papers have been published on various applications within this frequency range, including detectors,[1] absorbers,[2] modulators,[3] and others. Due to the absence of natural materials with appropriate electromagnetic responses in the terahertz (THz) range, most devices operating in this region have been designed using metamaterials.

Metamaterials are synthetic structures designed with unit cells smaller than the wavelength of the incident light, exhibiting distinctive electromagnetic characteristics absent in natural materials. Despite their unusual behavior, these characteristics are in accordance with established physical laws. Metamaterials are categorized into several types based on their specific properties. For instance, materials characterized by negative values of μ and ϵ demonstrate unique features like left-handed wave propagation and negative refractive index (RI) within the microwave spectrum. Initially, Veselago introduced the concept of materials exhibiting a negative RI, now known as double-negative (DNG) materials. Another class of materials, called Electromagnetic Band Gap (EBG), consists of periodic metallic, dielectric, or hybrid structures. These structures inhibit the propagation of electromagnetic waves over a defined frequency band, independent of the incident angle or polarization. As a result, metamaterials can be utilized to enhance the performance of antennas, filters, and absorbers in the microwave band.[4–6]

The advancement of metamaterials into the terahertz, infrared, and visible frequency domains has led to the realization of extraordinary properties, including cloaking, negative indices, reverse Doppler effects, and highly efficient absorption.[7,8] Among these, absorbers have garnered significant attention for their applications in sensor design, modulators, and solar cells.

In the THz frequency range, due to the use of metallic resonators, the intrinsic losses in metamaterials increase, reducing their performance. With the rapid advancements and excellent applications in fundamental physics, graphene has emerged as a potential replacement for traditional metallic materials. It provides a suitable platform for surface plasmons and the design of a perfect metamaterial absorber.[9,10] Reference 9 proposed a tunable dual-mode graphene absorber that achieves efficient THz absorption and sensing, demonstrating its potential for high-performance photonic applications.

An analytical approach for a graphene-based RI sensor with high accuracy is presented in Ref. 10, offering a theoretical foundation for precise THz sensing designs.

Graphene surface plasmons can exhibit strong confinement properties.[11–13] In contrast to surface plasmon polaritons in noble metals like silver and gold, graphene plasmons provide enhanced field localization with minimal optical attenuation. These features allow them to confine light to

---

*Corresponding author.

nanoscale wavelengths, thereby enhancing light absorption.[14] In addition to their superior confinement, graphene plasmons offer the unique benefit of dynamic tunability of the chemical potential by applying an external gate voltage — a feature not available in traditional metallic plasmonic systems.[15,16]

Since the wave vector of graphene plasmons is directly linked to the surface conductivity of graphene — which in turn is governed by its chemical potential — the application of an external gate voltage enables dynamic tuning of plasmonic absorber performance without altering the geometry.[17,18]

Currently, metamaterial absorbers are widely recognized for their utility in applications such as detection, security, and communications, and have become an active topic of research in the terahertz frequency range.[19,20] Landy *et al.* were the pioneers in introducing a metamaterial absorber capable of achieving perfect absorption.[21] Following this development, numerous metamaterial absorbers have been designed to operate across a wide frequency range, from microwave to infrared.[22–24]

In the terahertz range, Tao and collaborators introduced the first narrowband absorber.[25] Subsequently, researchers have employed different methods to achieve dual-band, broadband, and multi-band perfect metamaterial absorbers based on graphene.[26–29] Multi-band perfect absorbers, in particular, allow for complete absorption at several discrete frequencies, making them ideal for multi-band sensing applications. In general, multi-band perfect absorbers can be realized using two primary design strategies. The first, referred to as the co-planar approach, integrates multiple resonators of varying sizes within a single planar structure.[30,31] The second approach involves vertically stacking alternating multilayered structures.[32,33] Nevertheless, neither method is optimal for designing a structure capable of achieving multi-band absorption. For instance, the co-planar approach inevitably increases the unit cell size of the desired absorber, while the multilayer design results in excessive thickness and a heavier structure. In recent years, some simpler arrangements have been proposed to obtain multiband absorption.[34,35] However, improvements are still needed to achieve wide-angle absorption with polarization-insensitive behavior.

In the past decade, significant advancements have been made in various fields towards developing optical sensor technology. Technologies designed at micro- and nanoscale dimensions, along with integrated circuits, have driven the development of faster, more powerful, and smaller sensors. In any sensor design, the ultimate goal is to achieve a simple, reliable, and highly sensitive mechanism that results in a cost-effective and portable product. Modern methods for sensor design often involve the utilization of fluorescence and surface plasmon resonance techniques.[36,37] Beyond THz absorbers, advances in plasmonic and optical filters have been reported, including highly miniaturized nanoplasmonic filters with tunable cut-off wavelengths[36] and polarization-insensitive graphene disk THz absorbers for breast cancer detection using deep learning.[37]

However, these methods face numerous limitations. For instance, their efficiency is relatively low, and in fluorescence-based sensors, the analyzed molecule often needs to be replaced. Surface plasmon resonance-based methods have addressed many of these challenges and have found remarkable applications in areas such as food safety diagnostics, molecular biological analyses, and pharmaceutical applications. Despite significant advancements in optical detection methods in recent years, sensors operating in the infrared range are nearly absent. Recently, terahertz technology-based methods have garnered attention for detecting biological materials in extremely small quantities.[38]

THz spectroscopy systems employ terahertz radiation to extract molecular spectral information that is not feasible in other frequency ranges because molecular rotational, vibrational, and translational modes are excited in the terahertz range. Unlike other spectroscopic techniques, terahertz tools measure the electric field profile, which, through Fourier transformation, provides both phase and amplitude data. This enables the determination of the RI and absorption coefficients. Terahertz sensors play a critical role in medical applications, including biological detection and chemical analysis of substances such as identifying proteins or human blood sugar levels, by leveraging changes in the RI. Recent studies have further advanced metamaterial and graphene-based absorbers for RI sensing. Reference 39 demonstrated sensitivity enhancement by incorporating silicon layers into metamaterial sensors, while Ref. 40 designed a tunable quad-band fan-shaped split-ring graphene absorber for THz sensing applications.

A dual-band, polarization-independent maze-shaped graphene absorber optimized for biomedical use was also proposed,[41] and Ref. 42 reported a polarization-insensitive THz biosensor capable of distinguishing glioma tissues. In addition, ultra-narrowband graphene sensors for precise RI detection have been introduced,[43] and plasmonic and photonic crystal band-gap structures have been developed for basal cell cancer detection.[44] Beyond graphene-based devices, ultra-high sensitivity plasmonic sensors using elliptical resonators and MIM waveguides have also been explored for RI detection.[45]

Generally, terahertz sensors based on metasurfaces often use changes in resonance frequency to identify the properties of a material. These sensors operate by measuring absorption levels at resonance frequencies within a specific frequency band, where higher sensitivity and Q-factor (quality factor) indicate greater precision in detection.

Consequently, the paper is structured into two primary sections. The first part introduces a dual-band absorber and investigates the physical nature of each absorption peak. To validate the result of the designed absorber, the transmission line model was analyzed for the designed structure, and the outcomes of this theory showed exceptional agreement with the results achieved from full-wave simulations. In the second part, this dual-band absorber proposed for use as an RI sensor was examined, and this absorber is used as an RI biosensor for the early detection of breast cancer.

Since each of the frequencies related to the absorption peak undergoes a slight shift with variations in the analyte RI, each frequency can be selectively used as an RI biosensor. In Sec. 2, the conductivity coefficient of graphene is investigated. Section 3 discusses the plan and introduction of the proposed absorber design. In Sec. 4, the results obtained from the proposed structure are examined. In Sec. 5, for the designed dual-band absorber, the transmission line method is investigated. In Sec. 6, the device fabrication process and measurement setup for the proposed sensor are discussed. In Sec. 7, the suggested RI sensor functionality is analyzed, and in the final section, the conclusion is stated.

2. Graphene Conductivity

The unique behavior of graphene is significantly influenced by its conductivity. Based on the Kubo equation, graphene's conductivity is composed of two components: intera-band conductivity and inter-band conductivity.

$$\sigma_g = \sigma_{\text{in}} + \sigma_{\text{inter}} = \frac{2e^2 k_B T}{\pi\hbar^2}\frac{i}{\omega + i\Gamma^{-1}}\ln\left[2\cosh\left(\frac{E_F}{2k_BT}\right)\right] + \frac{e^2}{4\hbar}\left[\frac{1}{2} + \frac{1}{\pi}\tan^{-1}\left(\frac{\hbar\omega - 2E_F}{2k_BT}\right) - \frac{i}{2\pi}\ln\frac{(\hbar\omega + 2E_F)^2}{(\hbar\omega - 2E_F)^2 + 4(k_BT)^2}\right]. \quad (1)$$

Here, e indicates the charge of an electron, k_B is the Boltzmann constant, T indicates the surrounding temperature (typically assumed as 300 K), $\hbar$ refers to the reduced Planck constant, and ω is the angular frequency of an incoming plane wave. The graphene Fermi level, denoted as E_F, and the average relaxation time, represented as Γ, play crucial roles in the material's behavior.

In the THz frequency band, the impact of in-band conductivity on graphene's overall electrical conductivity is negligible. However, when graphene is highly doped, the condition $E_F \gg k_BT$ must be satisfied to simplify the analysis using the Drude formula. This approximation is particularly useful in understanding graphene's electrical properties under these conditions.

$$\sigma_g = \left(\frac{e}{\hbar}\right)^2 \frac{E_F}{\pi}\frac{i}{\omega + i\Gamma^{-1}} \quad (2)$$

The carrier relaxation time, denoted as Γ, is defined by the formula $\Gamma = (\mu E_F)/(e v_F^2)$, where v_F represents the Fermi velocity, set at 1.1×10^6 m/s. The parameter μ refers to the carrier mobility, which is an experimentally measured constant with a stable value of 3000 cm^2/(V···).

Figure 1 shows that the chemical potential of the graphene layer is regulated using a top-gate configuration. The method of top gate used in this configuration, specifically for a graphene-based terahertz absorber, involves electrostatic gating to precisely tune the graphene chemical potential (E_F). This approach utilizes the distinctive electronic characteristics of graphene along with the strong electric field produced by the ion-gel top gate. This top-gate structure applies a voltage V_{TG} across the ion-gel dielectric layer. This creates an electric field that induces charge carriers in a graphene sheet. This charge density directly shifts the Fermi level (E_F) of graphene, altering its electronic and optical properties.

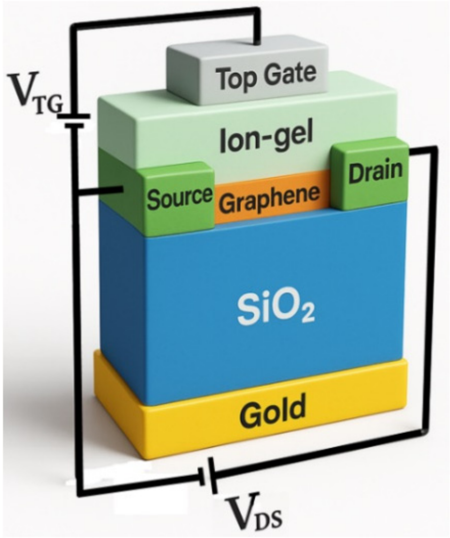

Fig. 1. Diagram of a top-gate configuration designed to control the graphene chemical potential.

Figures 2(a) and 2(b) illustrate the dependency of the components of graphene's electrical conductivity (both real (Re) and imaginary (Im) parts) on different values of chemical potential. It highlights that changes in frequency result in corresponding alterations in both the imaginary and real parts of the conductivity. These changes play a critical role in system performance by affecting resonance shifts over a wide range and adjusting the resonance amplitudes. Both the resonance shifts and amplitude modulation are directly tied to the imaginary and real conductivity components of graphene.

3. Structure Design

Figure 3 illustrates the unit cell design for the planned absorber. The scheme is composed of three distinct layers. The top layer features patterned graphene, while the middle layer consists of silicon dioxide (SiO2), a dielectric medium characterized by a dielectric constant of 2.25. The bottom layer is a gold plate with an electrical conductivity of 4.56 × 107 S/m. As seen in Fig. 3, the graphene pattern on the planned structure involves a square-shaped ring in which two rectangles are placed crosswise. Additionally, there are four circular rings in the space between the two rectangles

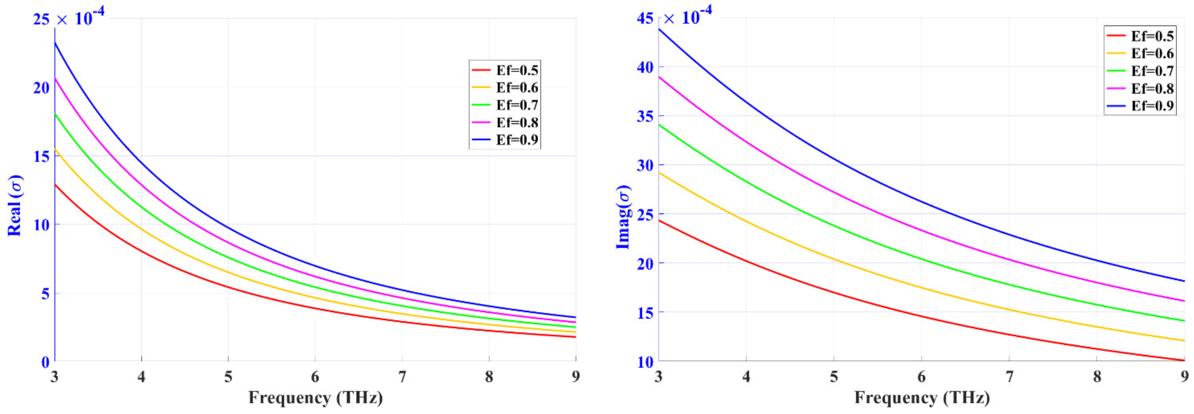

(a) (b)

Fig. 2. The conductivity of graphene for various chemical potentials. (a) Real part and (b) imaginary part

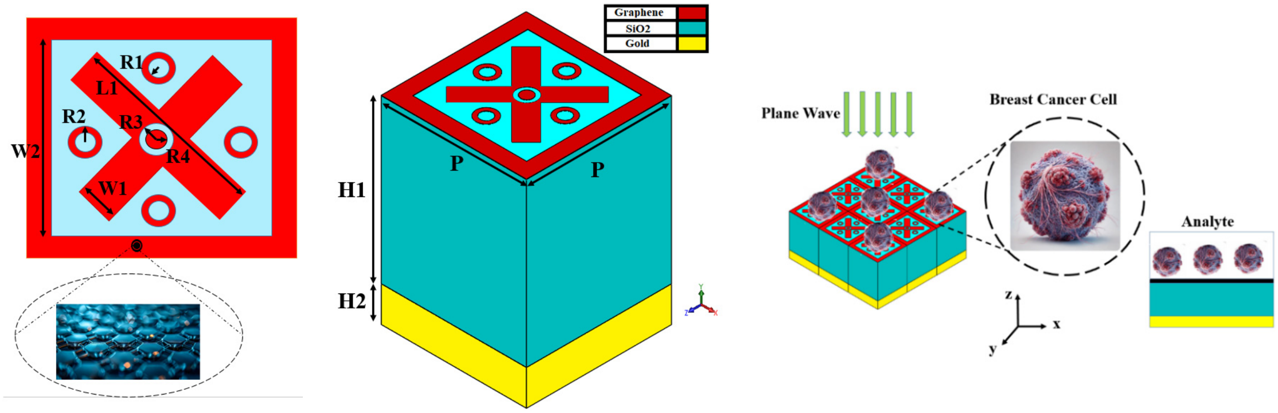

(a) (b) (c)

Fig. 3. The unit cell scheme for the designed absorber: (a) 2D front, (b) 3D visualization, and (c) proposed RI sensor.

and one circular ring at the intersection of the two rectangles. Figure 3(a) represents the top view, and Fig. 3(b) shows a 3D view of the planned absorber. Figure 3(c) is a graphical pattern intended to illustrate the performance of the proposed RI sensor, and it does not represent real-world performance. An analyte material (substance under test) is placed on the proposed absorber structure, and by altering the RI of the analyte material and measuring the shift of the peak frequency in the absorption diagram of the planned absorber, cancer cells can be identified. The designed structure dimensions are listed in Table 1.

Graphene contains free electrons capable of interacting with electromagnetic fields at terahertz frequencies. When electromagnetic waves strike the surface of graphene, their electric field excites the free electrons within the material. This excitation leads to the collective oscillation of electrons, known as plasmons. For efficient coupling between the electromagnetic waves and graphene's free electrons, the wave frequency must align with the natural oscillation frequency of the electrons in graphene. This alignment is typically achieved at terahertz frequencies. When this coupling occurs effectively, the electromagnetic wave energy is transferred to plasmonic oscillations on the graphene surface.[36] At the boundary between graphene and the dielectric material, these oscillations appear as surface plasmons. Surface plasmons are oscillations of the collective electrons confined to the graphene surface and localized near the graphene-dielectric boundary.

Before employing a metamaterial perfect absorber for sensing applications, it is essential to conduct a comprehensive

Table 1. Parameters value for designed absorber (unit: nm).

Parameter	Value (μm)	Parameter	Value (μm)
$H1$	4.6	$L1$	3.4
$H2$	1	$R1$	0.1
P	4	$R2$	0.2
$W1$	0.63	$R3$	0.2
$W2$	3	$R4$	0.1

evaluation of its unit cell performance. This includes verifying that the desired structure attains the required absorption features, such as high efficiency, and fulfills essential criteria, including sensitivity, stability, and repeatability. A comprehensive evaluation of the unit cell's performance is essential to confirm its appropriateness and reliability for sensing applications.

The designed structure underwent detailed analysis using CST software through full-wave simulation. CST provides precise analysis of electromagnetic properties, enabling an accurate assessment of the structure's performance and behavior. This analysis included a thorough examination of the absorber's electromagnetic properties, absorption characteristics, and other relevant parameters. The FDTD technique was utilized for the simulation, with appropriate boundary conditions applied: unit cell boundaries in the *X*- and *Y*-axes, and an open boundary condition in the *Z*-axis. This configuration ensures reliable simulation results, effectively validating the absorber's performance.

4. Results and Discussions

In graphene-based terahertz absorbers, electromagnetic waves are categorized into two fundamental modes: Transverse Electric (TE) and Transverse Magnetic (TM). These modes are characterized by the relative orientation of the electric and magnetic fields with respect to the wave propagation direction. In TE mode, the electric field is completely transverse to the wave propagation direction, with no component present along the propagation axis. Conversely, in the TM mode, the magnetic field is entirely transverse to the direction of propagation, with no component along the wave axis. Figure 4 illustrates the absorption diagram of the designed absorber. The graph represents the performance of the graphene pattern under the following conditions: a 0.95 eV chemical potential, a 1 ps relaxation time, and a 300 K temperature.

In Fig. 4, the absorption behavior of the planned absorber is presented, showcasing its performance as a dual-band absorber. It exhibits two separate absorption peaks at frequencies of 4.58 THz and 6.25 THz. The absorption rate of the designed structure at the frequency of 4.58 THz is 99.99%, and the absorption rate at the frequency of 6.25 THz is 90%.

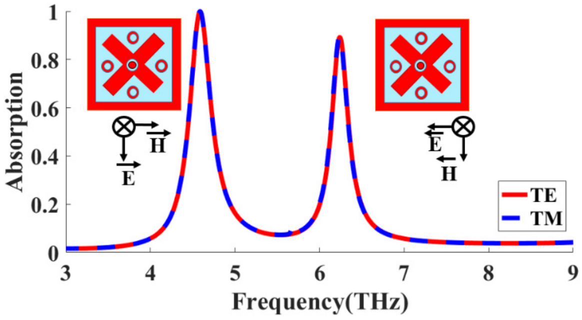

Fig. 4. The absorption behavior of the planned absorber.

This shows that the planned structure is polarization-insensitive and operates independently of the incident wave polarization angle. The planned structure incorporates a graphene pattern to enable tunability. Figure 5(a) demonstrates the absorption diagram of the planned structure for different chemical potentials of graphene. As shown, increasing the μc from 0.35 eV to 0.95 eV results in an amplitude reduction of the absorption peaks. The highest absorption peak and the optimal functionality of the structure are observed when μc is set to 0.95 eV. Figure 5(b) displays the 2D- and 3D-views of the absorption diagram versus changing chemical potential.

The abnormal absorption peak observed at higher frequencies in Fig. 5(a) can be explained by the excitation of higher-order plasmonic resonances in the patterned graphene structure and the enhanced interaction between the graphene layer and the dielectric substrate. As the frequency increases, nonfundamental modes arise from the coupling between localized surface plasmons and the periodicity of the unit cell, producing additional peaks beyond the primary dual-band absorption. Moreover, at higher frequencies, stronger coupling with the SiO2 spacer may induce slight impedance mismatches and Fabry–Pérot-like effects, further contributing to spurious resonances. It is important to note that these additional peaks do not compromise the sensing performance in

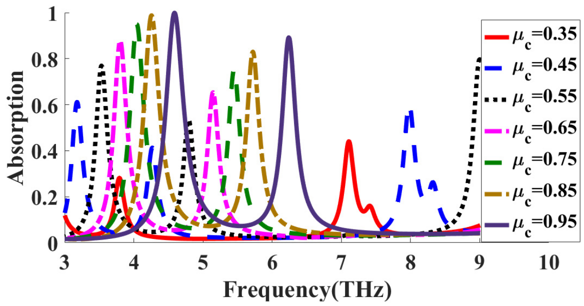

(a)

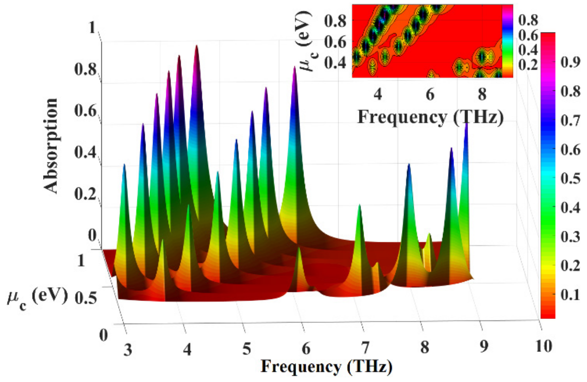

(b)

Fig. 5. (a) 2D Absorption diagram of the designed absorber with different chemical potentials. (b) 3D view of the absorption diagram versus changing the chemical potential.

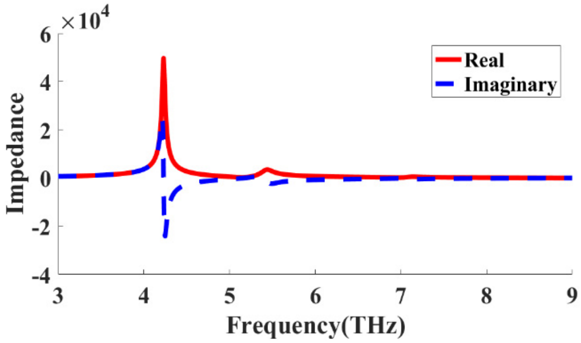

Fig. 6. Calculated normalized impedance curve for a planned absorber.

the operating bands (around 4.6 THz and 6.2 THz), where the absorber maintains stable resonance, high absorption, and excellent RI sensitivity. The designed structure demonstrates two distinct peaks of absorption with amplitudes near unity, indicating excellent impedance matching at these frequencies with the free space impedance of 377 Ω.

To analyze this phenomenon, Fig. 6 presents both components of the structure's impedance. At the desired frequencies associated with the absorption peaks the impedance approaches approximately $377 + j0$ ohms. This alignment demonstrates an effective impedance match between the designed absorber and the impedance of free space.

Figure 7 displays the electric field distributions, which reveal the physical mechanism of the planned absorber. The distribution is presented from the top view for each absorption frequency.

When an electromagnetic wave interacts with the absorber structure, surface plasmon modes are excited on the graphene surface, contributing to the absorption process. As displayed in Fig. 7(a), at a frequency of 4.58 THz, the electric field is strongly concentrated near the central regions of the structural elements. This indicates the presence of localized surface plasmon resonance (LSPR), where the electric field intensifies around the edges of the graphene structures. At a frequency of 6.25 THz, the electric field is more uniformly distributed across the entire structure, with lower intensity in the central regions compared to the lower frequency (Fig. 7(a)). This suggests that the mechanism of absorption is dominated by geometric resonance.

The angular orientation of the planned absorber relative to the incident wave direction is a critical factor in terahertz absorber design. Unlike conventional absorbers, the graphene-based structure exhibits a dependency on the polarization of the incident wave. Figure 8 presents an absorption diagram of the designed absorber across incident angles ranging from 0° to 90°, illustrating how its absorption characteristics change with varying angles. The absorption peak amplitudes diminish as the incident angle increases, demonstrating the structure's sensitivity to the incident wave angle. Unlike certain terahertz absorbers that are polarization-independent, the absorption peaks of this absorber are influenced by the polarization angle of the incident wave. Figure 8(b) shows the 2D- and 3D-views of the absorption diagram for various incident wave angles.

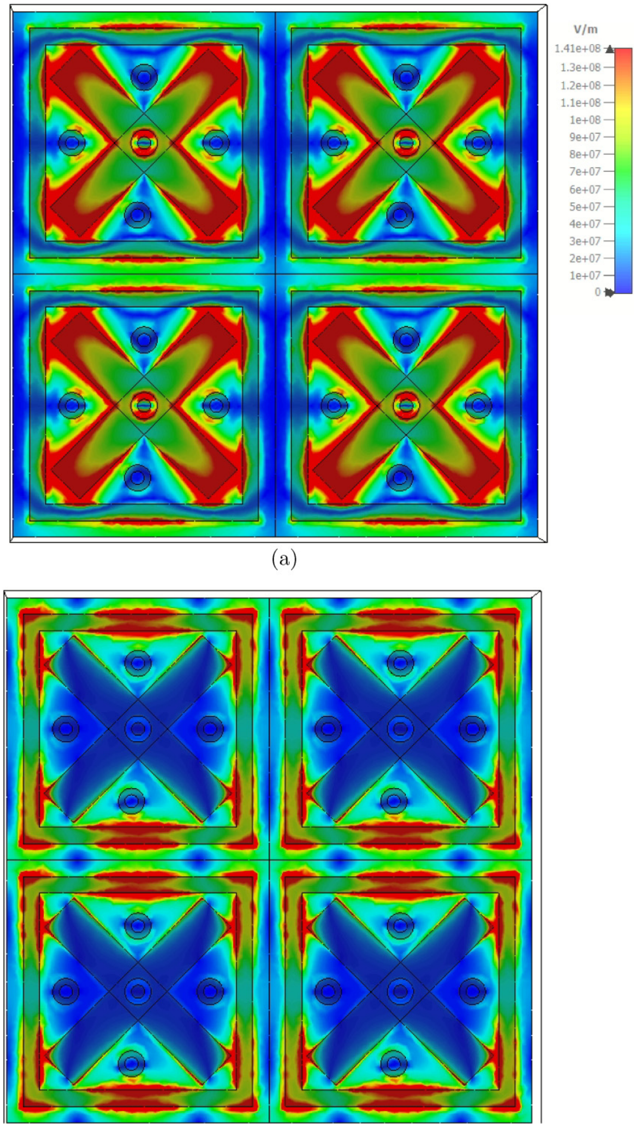

(a)

(b)

Fig. 7. The electrical field distribution of the planned absorber (a) 4.58 THz and (b) 6.25 THz.

The polarization-insensitive and wide-angle absorption of the proposed design is primarily attributed to the structural symmetry of the unit cell and the plasmonic confinement of graphene.

The absorber employs a symmetric square-ring geometry integrated with cross-placed rectangular strips and circular resonators, ensuring that the electromagnetic response remains nearly identical for both TE and TM polarizations. Consequently, the absorption peaks at 4.58 THz and 6.25 THz are preserved regardless of polarization angle. Furthermore, numerical simulations performed for incidence angles up to 50° confirmed that absorption at both resonance

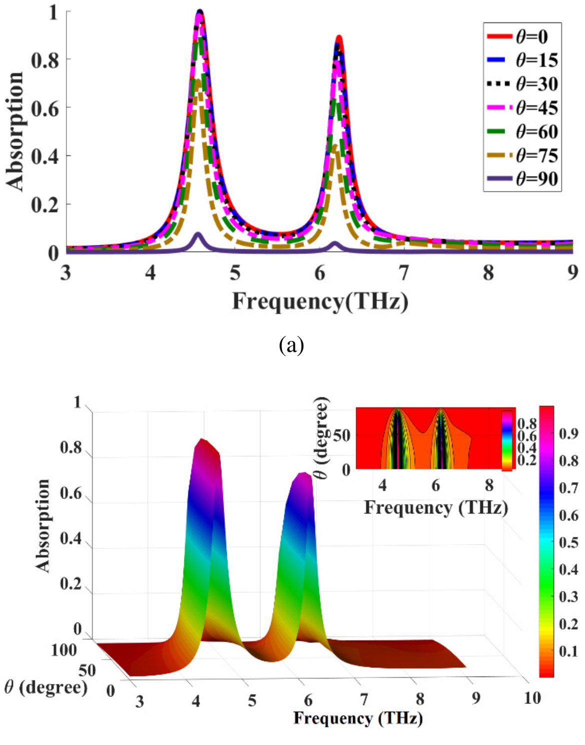

(a)

(b)

Fig. 8. The absorption diagram for various angles of received wave: (a) 2D and (b) 3D.

frequencies remains above 80%, demonstrating the wide-angle stability of the structure. This improvement arises from the strong plasmonic confinement in graphene and the coupling between multiple resonant elements, which minimizes angular sensitivity. In contrast to many previously reported absorbers with asymmetric geometries that exhibit strong polarization or angular dependence, the rotationally symmetric configuration of our proposed absorber achieves robust polarization insensitivity and stable performance over a wide range of incident angles.

5. Numerical Analyses of the Planned Absorber

To authenticate the full-wave software simulation outcomes and ensure the functionality of the planned absorber, we presented the TLM for the planned structure. The planned TLM is defined in Fig. 9. In the presented model, the gold layer acts as a short circuit, and the dielectric layer is modeled as a transmission line. The graphene layer is also modeled as a set of series resonators that are parallel to each other. Since this structure is dual-band, the graphene layer is modeled as two parallel branches of the series resonator.[65]

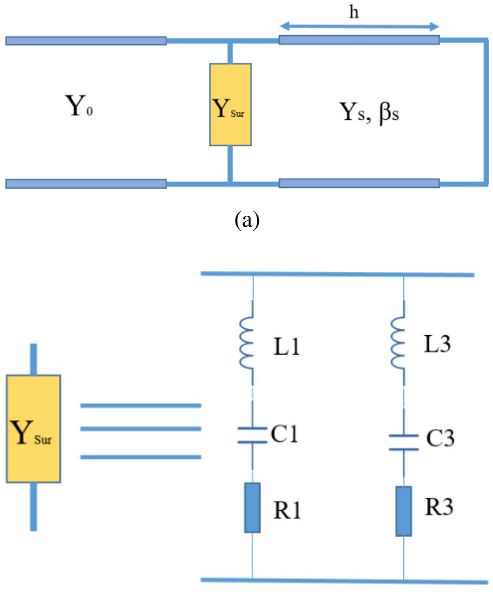

(a)

(b)

Fig. 9. The proposed TLM of the planned absorber.

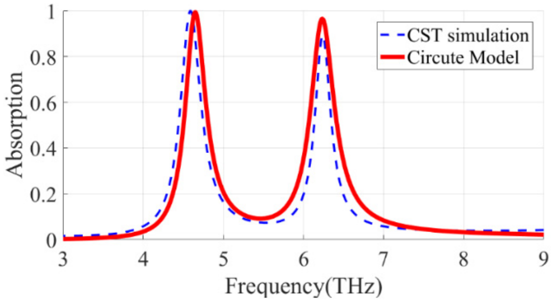

Fig. 10. Comparison results between CST software simulation (full-wave) and circuit model (transmission line model).

The calculation relationships of the model of the transmission line are given below. The comparison of the obtained results from the software simulation and the transmission line method is displayed in Fig. 10. The close agreement between the simulation outcomes and the TLM results validates the reliability and efficiency of the designed absorber.

In this model, the graphene pattern of the designed absorber is modeled with resonators that indicate with Y_{sur} that calculated from the following equation:

$$Y_{\text{sur}} = \sum_{n=1(\text{odd})}^{\infty} \left(R_n + jL_n\omega + \frac{1}{jC_n\omega}\right)^{-1} \tag{3}$$

where Y_{sur} represents the surface admittance. The equivalent resistor, inductor, and capacitor are calculated as follows:

$$\begin{aligned} R_n &= \frac{L}{S_n^2}\text{Re}\{\sigma_g^{-1}\}, \\ L_n &= \frac{L}{S_n^2}\frac{\text{Im}\{\sigma_g^{-1}\}}{\omega}, \\ C_n &= \frac{S_n^2}{L}\frac{2\varepsilon_{\text{eff}}}{q_n}. \end{aligned} \tag{4}$$

The propagation constant is calculated from Eq. (5), where k_0 is the vector of wave and n_s is the RI of the dielectric used in the proposed absorber.

$$\beta_s = k_0 n_s \tag{5}$$

$$Y_s = \frac{n_s}{\eta_0} \tag{6}$$

The free space impedance is equal as followws:

$$\eta_0 = 120\pi \tag{7}$$

$$k_0 = \frac{\omega}{c} \tag{8}$$

where ω is the angular frequency and c is the light speed in vacuum. The seen impedance from free space to graphene is calculated as follows:

$$Y_{in} = Y_{\mathrm{sur}} - jY_s \cot(\beta_s h), \tag{9}$$

$$\begin{aligned} Y_{in} = {} & \left(R_1 + jL_1\omega + \frac{1}{jC_1\omega}\right)^{-1} \\ & + \left(R_3 + jL_3\omega + \frac{1}{jC_3\omega}\right)^{-1} - jY_s\cot(\beta_s h), \end{aligned} \tag{10}$$

$$\begin{aligned} Y_{in}|_{\omega=\omega_1} = {} & \left(R_1 + jL_1\omega_1 + \frac{1}{jC_1\omega_1}\right)^{-1} \\ & - jY_s\cot(\beta_s h)|_{\omega=\omega_1}, \end{aligned} \tag{11}$$

$$\begin{aligned} Y_{in}|_{\omega=\omega 2} = {} & \left(R_1 + jL_1\omega_2 + \frac{1}{jC_1\omega_2}\right)^{-1} \\ & + \left(R_3 + jL_3\omega_2 + \frac{1}{jC_3\omega_2}\right)^{-1} \\ & - jY_s\cot(\beta_s h)|_{\omega=\omega_2}, \end{aligned} \tag{12}$$

$$\begin{aligned} \beta_s h|_{\omega=\omega_2} &= \pi/2, \\ L_3 C_3 &= \frac{1}{\omega_2^2}, \\ R_3 &= \eta_0/\alpha, \end{aligned} \tag{13}$$

$$\sigma_g = \frac{e^2 E_F \tau}{\pi\hbar^2}\frac{1}{1 + j\omega\tau} \tag{14}$$

$$\begin{aligned} R_n &= \frac{L}{S_n^2}\frac{\pi\hbar^2}{e^2 E_F \tau}, \\ L_n &= \tau R_n, \\ C_n &= \frac{S_n^2}{L}\frac{2\varepsilon_{\mathrm{eff}}}{q_n}. \end{aligned} \tag{15}$$

The condition to have a good impedance matching between the free space impedance and the designed absorber is

$$|S_{11}| = \left|\frac{1 - Y_{in}\eta_0}{1 + Y_{in}\eta_0}\right| < 0.22, \tag{16}$$

$$\mathrm{Im}(Y_{in})|_{\omega=\omega_1} = 0,$$

Table 2. Values of the parameters obtained from the transmission line model.

Parameter	Value	Parameter	Value
$R1$	121.6 Ω	$C1$	6.54×10^{-18}
$R2$	121.6 Ω	$C2$	3.61×10^{-18}
$L1$	0.135 nH	τ	1 Ps
$L2$	0.135 nH	$\mu\ c$	0.95 eV

$$\mathrm{Re}(Y_{in})|_{\omega=\omega_1} = \frac{1}{\eta_0}$$

$$\frac{L_1\omega_1\left(1 - \frac{1}{L_1C_1\omega_1^2}\right)}{R_1^2 + L_1^2\omega_1^2\left(1 - \frac{1}{L_1C_1\omega_1^2}\right)^2} + Y_s\cot(\beta_s h)|_{\omega=\omega_1} = 0, \tag{17}$$

$$\frac{R_1}{R_1^2 + L_1^2\omega_1^2\left(1 - \frac{1}{L_1C_1\omega_1^2}\right)^2} = \frac{1}{\eta_0}$$

$$\frac{\omega_1}{\omega_2} = \frac{2}{\pi}\cot^{-1}\left(\frac{1}{n_s}\sqrt{\frac{\alpha S_1^2}{S_3^2} - 1}\right) \tag{18}$$

The parameter values obtained from the transmission line method are also given in Table 2.

6. Device Fabrication and Measurement Setup

The detailed preparation steps, as illustrated in Fig. 11, are outlined below:

Graphene Synthesis and Transfer: Graphene is grown on a copper foil layer using the conventional chemical vapor deposition (CVD) technique. The copper foil is initially removed to facilitate the transfer of graphene onto the target substrate.

The process begins with spin-coating a PMMA layer onto a graphene/copper substrate. The copper is subsequently dissolved in an FeCl3 solution, after which the remaining PMMA/graphene layer is transferred into acetone to remove the PMMA.[66]

Metal substrate preparation: A 1000 nm gold film is sputter-coated onto the SiO2 wafer to create the desired metal

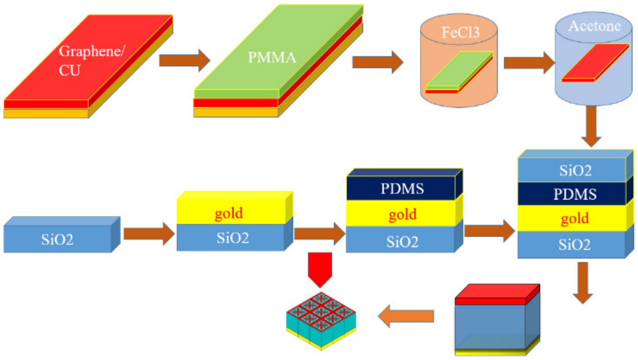

Fig. 11. The detailed preparation steps of graphene-based sensor.

substrate. A PDMS film layer with excellent adhesion is then applied to the gold substrate, and an SiO2 layer is fixed on top.

Graphene placement and patterning: The prepared graphene is transferred onto the fabricated SiO2/gold substrate. Laser direct-writing lithography is then used to create various graphene patterns on the substrate.

For optical measurements, a setup similar to that described in Ref. 64 can be used. The setup comprises a CCD camera, a beam splitter, a THz pump laser, a focusing lens, an objective lens, an optical signal analyzer (OSA), and a polarizer.

The process involves:

(1) Generating a broadband THz wave with the THz pump laser.
(2) Collimating the wave through a lens and adjusting polarization (vertical or horizontal) with a polarizer.
(3) Splitting the optical beam into two parts of uniform intensity using a beam splitter. One wave is directed to a CCD camera through a lens, and the other is sent to the objective lens and target device.

The OSA measures the reflected wave, which changes when different biomolecule concentrations are applied to the device. This setup enables the characterization of the device's performance for sensing applications.

7. Proposed Absorber Sensing Performance

To evaluate the performance of the planned absorber for sensing applications, an analyte (substance under test) is placed on the absorber. By varying the analyte RI from 1.1 to 1.6, a noticeable shift in the absorption peaks of the structure is observed. This behavior demonstrates the designed absorber's sensitivity to changes in the analyte's RI, highlighting its potential for use in selective sensing applications. Figure 12 depicts the designed absorber absorption diagram, illustrating its response to variations in the analyte RI. To check the performance of the RI sensor, there are some main parameters that should be checked for the proposed structure.

A suitable RI sensor should have high sensitivity (S), which indicates the absorption frequency shift or reflection peaks (Δf) per unit variation in the RI (Δn).

The formula for sensitivity is $s = \frac{\Delta f}{n}$ which Δf is the shift of the frequency, and Δn is the variation of RI. Sensitivity allows the detection of very small changes in the analyte RI.

Another important parameter is the Figure of Merit (FoM), representing the ratio between the sensor's sensitivity and its FWHM. The formula is $\mathrm{FoM} = \frac{S}{\mathrm{FWHM}}$, where S is sensitivity, and FWHM is the width of the absorption peak. A smaller FWHM results in a higher FoM, enabling the sensor to detect small RI changes with greater precision.

Another important parameter is the Q-factor, which should also be high. This represents the sharpness and clarity of the absorption or reflection peaks and is calculated as $= \frac{f}{\mathrm{FWHM}}$, where f is the peak frequency. The main parameters for the designed RI sensor are given in Table 3.

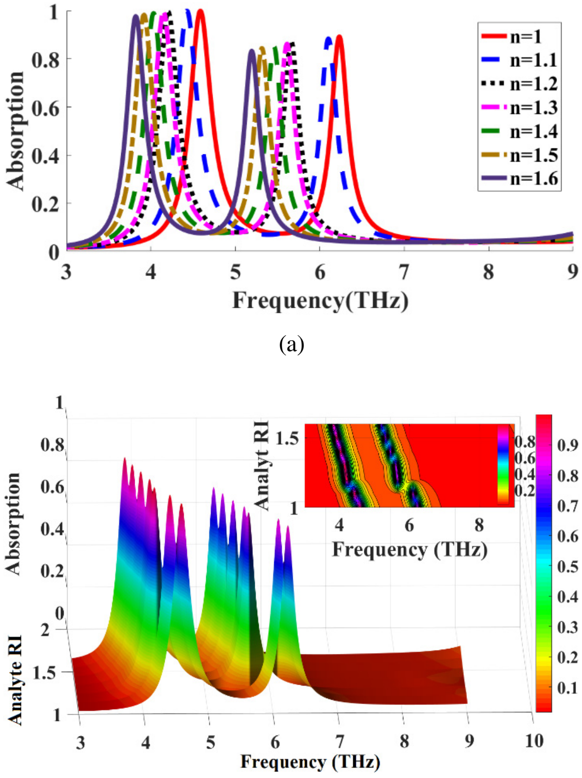

(a)

(b)

Fig. 12. The absorption diagram of the planned sensor: (a) 2D and (b) 3D.

In Fig. 12, the sensing experiment was modeled by approximating breast cells as a thin analyte layer deposited on the graphene metasurface. The analyte was represented by a 100-nm uniform film with its RI systematically varied from 1.0 to 1.7, covering the biologically relevant values of MCF10A ($n \approx 1.387$) and MCF7 ($n \approx 1.401$). The metasurface was designed with patterned graphene on a SiO2 spacer ($\varepsilon r \approx 2.25$, thickness $\approx 4.6\,\mu$m), backed by a gold ground plane ($\sigma \approx 4.56 \times 107$ S/m, thickness $1\,\mu$m). The graphene conductivity was calculated using the Kubo

Table 3. Designed features of planned biosensor.

RI	Frequency [THz]	S[THz/RIU]	FWHM [THz]	FoM	Q-factor
1	4.593	—	0.312	—	14.72
1.1	4.431	1.62	0.306	5.29	14.48
1.2	4.209	2.22	0.288	7.7	14.61
1.3	4.143	0.66	0.288	2.29	14.38
1.4	4.035	1.08	0.27	4	14.94
1.5	3.921	1.14	0.27	4.22	14.52
1.6	3.819	1.02	0.258	3.95	14.8

formula with a chemical potential of 0.95 eV, a relaxation time of 1 ps, and a temperature of 300 K. Electromagnetic excitation was applied at normal incidence within the 3–9 THz range, using periodic boundary conditions in the x–y directions and open boundaries in the z direction. The absorption spectra were obtained as $A = 1 - |S11|^2 - |S21|^2$, which simplifies to $A \approx 1 - |S11|^2$ due to the gold ground eliminating transmission. These parameters ensured that the simulation accurately reflected the operational environment for distinguishing between normal breast cells (MCF10A) and cancer cells (MCF7).

In addition, the mesh properties used in the simulations showed a tetrahedral high-frequency mesh with 7888 elements, minimum and maximum edge lengths of 0.0247 and 7.1316, and an average quality of 0.7085. Together, these details confirm the robustness of the numerical model and ensure reliable evaluation of the sensing performance.

In practical biosensing applications, one of the most common approaches for placing breast cancer cells or their biological content onto metasurfaces is the cell lysate method. In this technique, breast cancer cell lines such as MCF-7 or MDA-MB-231 are cultured, harvested, and subjected to controlled lysis using mild detergents or enzymatic buffers. After centrifugation to remove cellular debris, the clear lysate enriched in proteins and nucleic acids is deposited as a thin biological film on the metasurface, either by drop-casting, spin-coating, or through microfluidic delivery. This thin uniform layer perturbs the local RI around the resonant structure, leading to measurable resonance shifts that differentiate between cancerous and normal cells. In our simulations, this process was modeled by a 0.1 μm analyte layer with refractive indices ranging from 1.0 to 1.6, covering biologically relevant values for breast cancer cells.[67] In addition, other studies have modeled cell placement differently; for example, Tan *et al.*[68] considered two hemispherical analytes on a graphene surface and analyzed the variation of the absorption response at different positions for normal and cancerous cells. Together, these studies confirm that both cell lysate deposition and hemispherical analyte modeling provide effective strategies for representing cell–metasurface interactions in graphene-based biosensing platforms (Table 4).

A higher Q-factor ensures sharper and more defined peaks, improving detection accuracy. The function comparison of the planned sensor compared to the RI sensors introduced by previous researchers is given in Table 3.

The proposed absorber employs a hybrid unit-cell configuration consisting of a square ring with cross-placed rectangular strips and multiple circular rings. While the geometry is more complex than some previously reported designs, this unique configuration enables the coexistence of two distinct absorption mechanisms — LSPR (at 4.58 THz) and geometric resonance (at 6.25 THz).

Also, according to Table 3, the proposed sensor achieves a maximum sensitivity of 2220 GHz/RIU (2.22 THz/RIU) with a FoM of 7.7 RIU^{-1} and an average Q-factor of ~ 14.5. Compared to previously reported dual-band absorbers, our design provides a clear performance advantage. For example, Refs. 55 and 62 demonstrated relatively high FoM values (46.8 and 106, respectively), but their sensitivities were limited to 127–152 GHz/RIU, nearly an order of magnitude lower than ours. Similarly, Ref. 57 reported a sensitivity of 540 GHz/RIU and Ref. 63 achieved 473 GHz/RIU, which are still ~ 4 times lower than our result. Even the most recent works, such as Ref. 41 with 1150 GHz/RIU sensitivity, reported a FoM of only 1.55, while our sensor simultaneously achieves higher sensitivity and significantly improved FoM, ensuring both sharp resonance and high detection accuracy. Importantly, unlike many earlier designs that were optimized for general RI variations, our sensor directly addresses the biologically relevant RI range of 1.3–1.4 for breast cancer cells, making it highly suitable for early-stage biomedical detection. These points collectively highlight the novelty and superiority of our work compared to the cited studies.

Table 4. The comparison table between reported sensors in the prior research and the designed sensor.

References	Published year	Frequency band [THz]	Sensitivity [GHz/RIU]	FoM [RIU^{-1}]
46	2012	0.2–0.3	225	—
47	2013	0–1.2	261	—
48	2013	3.7	130	1.04
49	2014	0.5–1	163	2.67
50	2014	0.4–3	261	—
51	2016	0–3	457	3.1
52	2016	0.71	220	1.1
53	2016	0.5–1	500	—
54	2017	1.77	638	—
55	2017	0.1–0.9	127	46.8
56	2019	3.82	160	62.82
57	2019	0–3	540	2.86
58	2019	0.6–1.2	85	—
59	2019	1.5–3	300	2.94
60	2019	0.8–1.2	280	—
61	2020	0.1–1.9	280	8.54
62	2021	1–2.4	152	106
63	2023	1.3	473	16.9
10	2024	3.24	726	2.69
41	2025	4–8	1150	1.55
Proposed	2025	4.593	2220	7.7

Another key distinction of our work compared to many of the studies listed in Table 3 is the explicit consideration of the fabrication process. While most previous works have primarily focused on theoretical design and numerical simulations, our paper provides a practical fabrication pathway, thereby enhancing the experimental relevance of the proposed device. Specifically, we describe the sequential steps, including graphene growth using CVD, PMMA-assisted transfer, gold film deposition on the SiO2 substrate, and laser direct writing lithography to pattern the graphene structure.

By presenting these detailed fabrication steps, we demonstrate that the proposed sensor is not only superior in terms of performance parameters (sensitivity, FoM, and *Q*-factor), but also technologically feasible for real-world implementation, which is rarely addressed in earlier dual-band absorber reports.

In addition to the demonstrated design and simulation results, considerations of long-term stability, environmental tolerance, and operational lifetime are crucial for the practical applicability of the proposed sensor. Graphene, compared with traditional metallic absorbers, inherently provides excellent chemical stability, mechanical robustness, and resistance to environmental degradation, suggesting favorable long-term performance. Moreover, the use of protective encapsulation layers such as SiO2 or PDMS can further shield the graphene surface from humidity, oxidation, and contamination, thereby improving durability and ensuring reliable sensing performance under real-world conditions. Although systematic experimental lifetime tests were not conducted in this study, the top-gate tunability of graphene enables reversible and repeatable operation without significant structural degradation, which represents a promising feature for extended use. Future work will therefore focus on experimental investigations of stability and lifetime to complement the present proof-of-concept demonstration and further validate the potential of the proposed device for biomedical sensing applications.

While this study is primarily simulation-based, we acknowledge the importance of transitioning the proposed sensor to real-world breast cancer diagnostic platforms. The next steps include developing a prototype for testing in medical and clinical settings, where we will assess factors like noise effects, fabrication tolerances, and biological interactions. The sensor will also be integrated with existing diagnostic technologies such as mammography and MRI to enhance diagnostic accuracy. Although we face challenges related to fabrication and testing, we are committed to addressing these limitations through experimental validation in future work, which will ensure the practical applicability of the sensor in real-world scenarios.

8. Conclusion

The proposed graphene-based dual-band absorber shows outstanding performance as an RI biosensor in the terahertz frequency range. It achieves high absorption efficiency, with peaks at 4.58 THz (99.99%) and 6.25 THz (90%), making it a promising dual-band sensor. The sensor demonstrates excellent sensitivity (up to 2.22 THz/RIU) and a FOM of 7.7 RIU^{-1}, with an average *Q*-factor of ~ 14.5, indicating sharp, well-defined absorption peaks. It is particularly effective for detecting breast cancer cell RI ranges (1.3 to 1.4), offering great potential for early diagnosis. The sensor's polarization-insensitive behavior and tunable chemical potential using a top-gate method enhance its reliability and versatility. However, the study is based on simulations, and experimental validation is necessary to verify the device's real-world performance. Future work will focus on experimental testing and addressing the challenges of transitioning the sensor to practical biomedical applications.

Acknowledgments

This research is funded by Semnan University. Also, the authors would like to thank the journal reviewers for their valuable comments.

Author Contributions

SAK: Conceptualization, methodology, investigation, software simulation, resources, writing — original draft, writing — review and editing. PR: Methodology, validation, writing — review and editing, supervision. MD: Methodology, validation, writing — review and editing.

Data Availability

All data generated or analyzed during this study are included in this published paper.

Funding

No funding was received for this research.

Conflict of Interest

The authors declare that they have no conflict of interest.

Ethical Approval

We declare that this paper is original, has not been published before, and is not currently considered for publication elsewhere. We confirm that the paper has been read and approved by all named authors and that there are no other persons who satisfied the criteria for authorship but are not listed. We further confirm that the order of authors listed in the paper has been approved by all of us.

Consent for Publication

Written informed consent for publication was obtained from all participants.

Consent to Participate

Written informed consent for participation was obtained from all participants.

ORCID

Seyed Amin Khatami https://orcid.org/0009-0007-1318-9497
Pejman Rezaei https://orcid.org/0000-0002-1266-3229
Mohammad Danaie https://orcid.org/0000-0001-7046-2794

References

[1] S. S. Dhillon *et al.*, The 2017 terahertz science and technology roadmap, *J. Phys. D: Appl. Phys.* **50**(4), 043001 (2017).

[2] S. A. Khatami, P. Rezaei and P. Zamzam, Quad band metal–dielectric–metal perfect absorber to selective sensing application, *Opt. Quantum Electron.* **54**(10), 638 (2022).

[3] H.-T. Chen *et al.*, Active terahertz metamaterial devices, *Nature* **444**(7119), 597 (2006).

[4] P. Umar *et al.*, A novel metamaterial electromagnetic band gap (MM-EBG) isolator to reduce mutual coupling in low-profile MIMO antenna, *J. Electron. Mater.* **51**(2), 626 (2022).

[5] C. Milias *et al.*, Metamaterial-inspired antennas: A review of the state of the art and future design challenges, *IEEE Access* **9**, 89846 (2021).

[6] J. Zhang, J. Arroyo and M. A. Lediju Bell, Multispectral photoacoustic imaging of breast cancer tissue with histopathology validation, *Biomed. Opt. Express* **16**(3), 995 (2025).

[7] D. Schurig *et al.*, Metamaterial electromagnetic cloak at microwave frequencies, *Science* **314**(5801), 977 (2006).

[8] S. A. Cummer *et al.*, Full-wave simulations of electromagnetic cloaking structures, *Phys. Rev. E, Stat. Nonlinear Soft Matter Phys.* **74**(3), 036621 (2006).

[9] N. Korani *et al.*, A tunable graphene dual mode absorber for efficient terahertz radiation absorption and sensing applications, *Diam. Relat. Mater.* **149**, 111554 (2024).

[10] S. A. Khatami, P. Rezaei and M. Danaie, High accuracy graphene-based refractive index sensor: Analytical approach, *Diam. Relat. Mater.* **146**, 111225 (2024).

[11] Z. Yi *et al.*, Nanostrip-induced high tunability multipolar fano resonances in a Au ring-strip nanosystem, *Nanomaterials* **8**(8), 568 (2018).

[12] A. H. Asl and M. Khajenoori, *Green Extraction in Separation Technology* (CRC Press, 2021).

[13] A. Vakil and N. Engheta, Transformation optics using graphene, *Science* **332**(6035), 1291 (2011).

[14] H. Li, J. Niu and G. Wang, Dual-band, polarization-insensitive metamaterial perfect absorber based on monolayer graphene in the mid-infrared range, *Results Phys.* **13**, 102313 (2019).

[15] J. Huang *et al.*, High sensitivity refractive index sensing with good angle and polarization tolerance using elliptical nanodisk graphene metamaterials, *Phys. Scr.* **94**(8), 085805 (2019).

[16] M. Huang *et al.*, Based on graphene tunable dual-band terahertz metamaterial absorber with wide-angle, *Opt. Commun.* **415**, 194 (2018).

[17] W. Li and Y. Cheng, Dual-band tunable terahertz perfect metamaterial absorber based on strontium titanate (STO) resonator structure, *Opt. Commun.* **462**, 125265 (2020).

[18] H. Luo and Y. Cheng, Thermally tunable terahertz metasurface absorber based on all dielectric indium antimonide resonator structure, *Opt. Mater.* **102**, 109801 (2020).

[19] F. Chen, Y. Cheng and H. Luo, A broadband tunable terahertz metamaterial absorber based on single-layer complementary gammadion-shaped graphene, *Materials* **13**(4), 860 (2020).

[20] S. K. Ghosh *et al.*, Tunable graphene-based metasurface for polarization-independent broadband absorption in lower mid-infrared (MIR) range, *IEEE Trans. Electromagn. Compat.* **62**(2), 346 (2019).

[21] N. I. Landy *et al.*, Perfect metamaterial absorber, *Phys. Rev. Lett.* **100**(20), 207402 (2008).

[22] S. Bhattacharyya *et al.*, Wide-angle broadband microwave metamaterial absorber with octave bandwidth, *IET Microw. Antennas Propag.* **9**(11), 1160 (2015).

[23] D. Yan and J. Li, Tunable all-graphene-dielectric single-band terahertz wave absorber, *J. Phys. D: Appl. Phys.* **52**(27), 275102 (2019).

[24] J. A. Mason *et al.*, Strong coupling of molecular and mid-infrared perfect absorber resonances, *IEEE Photonics Technol. Lett.* **24**(1), 31 (2011).

[25] H. Tao *et al.*, A metamaterial absorber for the terahertz regime: Design, fabrication and characterization, *Opt. Express* **16**(10), 7181 (2008).

[26] P. Fang *et al.*, Single-and dual-band convertible terahertz absorber based on bulk Dirac semimetal, *Opt. Commun.* **462**, 125333 (2020).

[27] M. Zhong *et al.*, Design and measurement of a single-dual-band tunable metamaterial absorber in the terahertz band, *Physica E* **124**, 114343 (2020).

[28] J. Wu, X. Liu and Z. Huang, Broadband light absorption with doped silicon for the terahertz frequency, *Opt. Laser Technol.* **119**, 105657 (2019).

[29] Z. Song *et al.*, Wide-angle absorber with tunable intensity and bandwidth realized by a terahertz phase change material, *Opt. Commun.* **464**, 125494 (2020).

[30] J. Xu *et al.*, Frequency-tunable metamaterial absorber with three bands, *Optik* **172**, 1057 (2018).

[31] B. Ma *et al.*, Novel three-band microwave metamaterial absorber, *J. Electromagn. Waves Appl.* **28**(12), 1478 (2014).

[32] F. Hu *et al.*, Design of a polarization insensitive multiband terahertz metamaterial absorber, *J. Phys. D: Appl. Phys.* **46**(19), 195103 (2013).

[33] B.-X. Wang *et al.*, Six-band terahertz metamaterial absorber based on the combination of multiple-order responses of metallic patches in a dual-layer stacked resonance structure, *Sci. Rep.* **7**(1), 41373 (2017).

[34] S. Hadipour, P. Rezaei and A. Norouzi-Razani, Multi band square-shaped polarization-insensitive graphene-based perfect absorber, *Opt. Quantum Electron.* **56**(3), 471 (2024).

[35] S. A. Khatami and P. Rezaei, Coupled mode theory analysis of the graphene-based multi-band superabsorber for selective sensing application, *Diam. Relat. Mater.* **158**, 112690 (2025).

[36] S. M. Ebadi and S. Khani, Highly-miniaturized nano-plasmonic filters based on stepped impedance resonators with tunable cut-off wavelengths, *Plasmonics* **18**(4), 1607 (2023).

[37] P. Zamzam, P. Rezaei, S. A. Khatami and B. Appasani, Super perfect polarization-insensitive graphene disk terahertz absorber for breast cancer detection using deep learning, *Opt. Laser Technol.* **183**, 112246 (2025).

[38] R. Cheng *et al.*, High-sensitivity biosensor for identification of protein based on terahertz Fano resonance metasurfaces, *Opt. Commun.* **473**, 125850 (2020).

[39] S. A. Khatami *et al.*, Smith chart analysis for transmission line method validation of a simple graphene-based absorber in sugar molecules detection, *Results Phys.* **77**, 108464 (2025).

[40] M.-R. Nickpay, M. Danaie and A. Shahzadi, Graphene-based tunable quad-band fan-shaped split-ring metamaterial absorber and refractive index sensor for THz spectrum, *Micro Nanostruct.* **173**, 207473 (2023).

[41] B. Khodadadi, P. Rezaei and S. Hadipour, Dual-band polarization-independent maze-shaped absorber based on graphene for terahertz biomedical sensing, *Opt. Express* **33**(3), 3869 (2025).

[42] X. Wu *et al.*, Design of a polarization-insensitive terahertz metamaterial biosensor for glioma tissue identification, *Biomed. Opt. Express* **16**(6), 2337 (2025).

[43] Q. Shangguan *et al.*, Design of ultra-narrow band graphene refractive index sensor, *Sensors* **22**(17), 6483 (2022).

[44] S. Khani and M. Hayati, Optical biosensors using plasmonic and photonic crystal band-gap structures for the detection of basal cell cancer, *Sci. Rep.* **12**(1), 5246 (2022).

[45] S. Khani and M. Hayati, An ultra-high sensitive plasmonic refractive index sensor using an elliptical resonator and MIM waveguide, *Superlattices Microstruct.* **156**, 106970 (2021).

[46] V. Astley *et al.*, Terahertz multichannel microfluidic sensor based on parallel-plate waveguide resonant cavities, *Appl. Phys. Lett.* **100**(23), 231108 (2012).

[47] L. Jy, Y. B. Liu and T. Peng, Hybrid terahertz plasmonic waveguide for sensing applications, *Opt. Express* **21**(18), 21087 (2013).

[48] C. Chen, Y. Yang and T. Yen, Unveiling the electromagnetic responses of four fold symmetric metamaterials and their terahertz sensing capability, *Appl. Phys. Express* **6**(2), 022002 (2013).

[49] L. Cong and R. Singh, Sensing with THz metamaterial absorbers, arXiv:1408.3711.

[50] F. Fan *et al.*, Terahertz refractive index sensing based on photonic column array, *IEEE Photonics Technol. Lett.* **27**(5), 478 (2014).

[51] X. Li *et al.*, Design of terahertz metal–dielectric–metal waveguide with microfluidic sensing stub, *Opt. Commun.* **361**, 130 (2016).

[52] X. Hu *et al.*, Metamaterial absorber integrated microfluidic terahertz sensors, *Laser Photonics Rev.* **10**(6), 962 (2016).

[53] A. Soltani *et al.*, Highly sensitive terahertz dielectric sensor for small-volume liquid samples, *Appl. Phys. Lett.* **108**(19), 191105 (2016).

[54] W. Zhang *et al.*, Ultrasensitive dual-band terahertz sensing with metamaterial perfect absorber, in *2017 IEEE MTT-S Int. Microwave Workshop Series on Advanced Materials and Processes for RF and THz Applications (IMWS-AMP)* (IEEE, 2017), pp. 1–3.

[55] W. Wang *et al.*, Experimental demonstration of an ultra-flexible metamaterial absorber and its application in sensing, *J. Phys. D: Appl. Phys.* **50**(13), 135108 (2017).

[56] F. G. Vanani *et al.*, Design of double ring label-free terahertz sensor, *IEEE Sens. J.* **19**(4), 1293 (2019).

[57] A. Keshavarz and Z. Vafapour, Sensing avian influenza viruses using terahertz metamaterial reflector, *IEEE Sens. J.* **19**(13), 5161 (2019).

[58] L. S. Li, F. Hu, Z. Chen, W. Zhang and J. Han, Metamaterial terahertz sensor for measuring thermal-induced denaturation temperature of insulin, *IEEE Sens. J.* **20**(4), 1821 (2019).

[59] A. S. Saadeldin *et al.*, Highly sensitive terahertz metamaterial sensor, *IEEE Sens. J.* **19**(18), 7993 (2019).

[60] Y. K. Srivastava *et al.*, Terahertz sensing of 7 nm dielectric film with bound states in the continuum metasurfaces, *Appl. Phys. Lett.* **115**(15), 151105 (2019).

[61] T. Chen *et al.*, Design of a terahertz metamaterial sensor based on split ring resonator nested square ring resonator, *Mater. Res. Express* **7**(9), 095802 (2020).

[62] Z. Li *et al.*, Three-band perfect absorber with high refractive index sensing based on an active tunable Dirac semi-metal, *Phys. Chem. Chem. Phys.* **23**(32), 17374 (2021).

[63] S. Barzegar-Parizi, Refractive index sensor with dual sensing bands based on array of Jerusalem cross cavities to detect the hemoglobin concentrations, *Opt. Quantum Electron.* **55**(1), 46 (2023).

[64] A. Liu *et al.*, Fabrication and characterization of integrable GaAs-based high-contrast grating reflector and Fabry–Pérot filter array with GaInP sacrificial layer, *IEEE Photonics J.* **8**(1), 2700509 (2016).

[65] S. Barzegar-Parizi and A. Khavasi, Designing dual-band absorbers by graphene/metallic metasurfaces, *IEEE J. Quantum Electron.* **55**(2), 1 (2019).

[66] S. Zhou, K. Bi, Q. Li, L. Mei, Y. Niu, W. Fu and X. Chou, Patterned graphene-based metamaterials for terahertz wave absorption, *Coatings* **13**(1), 59 (2022).

[67] V. Singh, A. Nand, J. Zhang and J. Zhu, Non-specific adsorption of serum and cell lysate on 3D biosensor platforms: A comparative study based on SPRi, *Arab. J. Chem.* **12**(8), 3038 (2019).

[68] C. Tan, S. Wang, S. Li, X. Liu, J. Wei, G. Zhang and H. Ye, Cancer diagnosis using terahertz-graphene-metasurface-based biosensor with dual-resonance response, *Nanomaterials* **12**(21), 3889 (2022).